Monthly Notices
of the
ROYAL ASTRONOMICAL SOCIETY

MNRAS **505,** 2177–2185 (2021)
Advance Access publication 2021 May 22

https://doi.org/10.1093/mnras/stab1426

Rovibrationally resolved direct photodissociation of MgO

Tianrui Bai,[1,2] Zhi Qin [2,3]★ and Linhua Liu[1,2,4]★

[1]*School of Energy and Power Engineering, Shandong University, Jinan, Shandong 250061, China*
[2]*Optics and Thermal Radiation Research Center, Institute of Frontier and Interdisciplinary Science, Shandong University, Qingdao, Shandong 266237, China*
[3]*School of information science and Engineering, Shandong University, Qingdao, Shandong 266237, China*
[4]*School of Energy Science and Engineering, Harbin Institute of Technology, Harbin, Heilongjiang 150001, China*

Accepted 2021 May 14. Received 2021 May 14; in original form 2021 February 25

ABSTRACT

The photodissociation process of magnesium oxide (MgO) may be a main source of the magnesium atom in planetary exospheres due to the impact events on planets. In this work, we calculated the state-resolved cross-sections of the photodissociation of MgO for the transitions from the full range of rovibrational levels of the $X^1\Sigma^+$ and $a^3\Pi$ states, where the photon wavelength ranged from 50 to 5000 nm. The applications of the state-resolved cross-sections to the local thermodynamic equilibrium (LTE) conditions were also investigated for the temperatures ranging from 500 to 10 000 K. Based on the calculated LTE cross-sections, the photodissociation rates in the interstellar, solar, and blackbody radiation fields were obtained as well. The rates in all studied radiation fields increase with the temperature increasing and are dominated by the $e^3\Sigma^- \leftarrow a^3\Pi$ and $F^1\Pi \leftarrow X^1\Sigma^+$ transitions. The knowledge of the photodissociation cross-sections and rates of MgO plays a key role in the investigations of the chemical behaviour of the alkaline-earth element Mg in planetary exospheres, atmospheres of cool stars, and envelopes of evolved stars.

Key words: astrochemistry – molecular data – molecular processes.

1 INTRODUCTION

Magnesium (Mg) is a key element for studying the evolution of cool stars and also plays an important role in studies of α-process nucleosynthesis in the Universe (Mashonkina 2013). As the most abundant cosmic metal, it has been observed in Mercury's exosphere during the MESSENGER's second flyby of Mercury (McClintock et al. 2009) and in Earth's upper atmosphere by optical spectrometers carried on satellites (Anderson & Barth 1971; Correira et al. 2008). Mg-bearing molecules have also been observed in other planets in the solar system (Bennett et al. 2013). For example, MgO was detected in the exosphere of Mercury (Sarantos et al. 2011; Stockstill-Cahill et al. 2012) and the lunar atmosphere during the 2009 Perseid meteor shower (Berezhnoy et al. 2014). According to the studies on the chemistry of impact events on Moon and Mercury (Berezhnoy 2013, 2018), it was found that MgO was formed in the impact-produced vapoor clouds after the meteoroid bombardment and then released to the exosphere. Finally it was destroyed by solar photons while on the ballistic trajectory (Berezhnoy 2010). Namely, the photodissociation of MgO may be a main source of Mg in planetary exospheres (Menelaos et al. 2011; Valiev et al. 2017), which can be expressed by

$$\mathrm{MgO} + h\nu \rightarrow \mathrm{Mg} + \mathrm{O}. \quad (1)$$

Photodissociation processes are found to be important to model the evolution of chemical composition in nearly every type of astrophysical region, from the edges of dense clouds close to bright young stars to the surface layers of protoplanetary discs and giant molecular clouds on galactic scales (Heays et al. 2017). Especially, for small molecules like MgO, the photodissociation process is the key destruction pathway in these regions, which affects the abundances of Mg and MgO in the interstellar medium. Meanwhile, this process can also generate chemically reactive radicals, opening pathways to the formation of Mg-bearing species (Sternberg & Dalgarno 1995; Lee et al. 1996; Li et al. 2014). Thus the quantitative modelling of photodissociation processes in clouds, envelopes and discs is a prerequisite for estimating the abundance of MgO and understanding the model of the magnesium chemistry (Plane & Whalley 2012).

Cross-sections and rate coefficients are main parameters of photodissocition processes and can be further used to investigate the behaviour of delivery of Mg to the exosphere in the impact-produced cloud. For example, to estimate the kinetic energies of photolysis-generated Mg and O atoms, the photodissociation cross-sections of MgO for four transitions were calculated by a simple estimate of vibrational wavefunctions (Valiev et al. 2016; Valiev et al. 2017). In order to more accurately describe the photodissociation process, Valiev et al. (2020) recently improved this model to obtain the photodissociation cross-sections of many diatomic melecules. However, the photolysis process of MgO was ignored. Thus, an accurate and comprehensive quantum chemistry method to calculate the MgO photodissociation is urgently required. Meanwhile, the wave functions for the unbound state in the improved model were characterized by an exponential repulsive potential curve (Valiev et al. 2020). However, the exponential curve was failed to completely characterize the potential of some high excited states because of the avoided crossings between the same symmetries. These states were

★ E-mail: z.qin@sdu.edu.cn (ZQ); liulinhua@sdu.edu.cn (LL)

important to investigate the photodissociation processes between the H Lyman limit and H Lyman α. For example, Pattillo et al. (2018) computed the photodissociation cross-sections of CS for the transitions from the ground electronic state to six excited electronic states, where the transition to the high excited state was dominant in the extreme ultraviolet region. This was also confirmed by the cross-sections of photodissocaion processes of CN, HeH^+, SH^+, and SiH^+ (Stancil et al. 1997; Miyake et al. 2011; El-Qadi & Stancil 2013; Mcmillan et al. 2016). In these calculation, the Numerov method was used to calculate the rovibrational wavefunctions of high excited states, which has also been used to compute the photodissociation cross-sections of a Mg-containing diatomic molecule, MgH (Weck et al. 2003). Thus, the goal of this work is to obtain more accurate rovibrationally resolved cross-sections and rates of the direct photodissociation of MgO, including as many transitions from high excited states to the $X^1\Sigma^+$ and $a^3\Pi$ states as possible.

In this work, the potential energy curves (PECs) for 12 states and the transition dipole moments for the transitions from the $X^1\Sigma^+$ and $a^3\Pi$ states are calculated by the *ab initio* methodology. Then, the state-resolved cross-sections are computed for the transitions from all rovibrational levels of the $X^1\Sigma^+$ and $a^3\Pi$ states and the local thermodynamic equilibrium (LTE) cross-sections are calculated for temperatures ranging from 500 to 10 000 K. Finally, the photodissociation rates in the interstellar, solar, and blackbody radiation field are analyzed.

2 METHODS

2.1 Potential energy curves and transition dipole moments

12 electronic states, including $5^1\Pi$, $4^1\Pi$, $F^1\Pi$, $G^1\Pi$, $E^1\Sigma^+$, $B^1\Sigma^+$, $A^1\Pi$, $X^1\Sigma^+$, $a^3\Pi$, $b^3\Sigma^+$, $c^3\Sigma^+$, and $d^3\Delta$ were taken into account for the photodissociation of MgO in this work, where the $X^1\Sigma^+$, $B^1\Sigma^+$, $A^1\Pi$, $a^3\Pi$, $b^3\Sigma^+$, $c^3\Sigma^+$, and $d^3\Delta$ states have been investigated in our previous work (Bai et al. 2020). The PECs and TDMs were calculated at the icMRCI/aug-cc-pCV5Z-DK level of theory as implemented in MOLPRO 2015 software package (Werner et al. 2015). As for the $B^1\Sigma^+$, $F^1\Pi$, and $G^1\Pi$ states, the PECs were calculated by the same level of theory in this work. But for the higher electronic states ($5^1\Pi$, $4^1\Pi$, and $E^1\Sigma^+$), the calculation of the PECs used the cc-pV5Z basis set and a larger active space including 12 molecular orbitals and six outer electrons. In addition, to obtain the PECs of these high excited states at the long internuclear distances, 10 electronic states ($X^1\Sigma^+$, $B^1\Sigma^+$, $5^1\Pi$, $4^1\Pi$, $F^1\Pi$, $G^1\Pi$, $A^1\Pi$, $D^1\Delta$, and $C^1\Sigma^-$) were considered in the state-averaged calculation, which was used as the reference for further MRCI calculations. To calculate cross-sections and rate coefficients, the PECs and TDMs were needed over the short and long range of internuclear distances R. For the large distances (>15 Å), the long-rage forms were used for the separating atoms. The PECs can be extrapolated by the following function at large distances

$$V(R) = -\frac{C_5}{R^5} - \frac{C_6}{R^6} + V(R \to \infty), \tag{2}$$

where C_6 is the dipole-dipole dispersion (van der Waals) coefficient and is calculated by the London formula

$$C_6 = \frac{3}{2}\frac{\tau_{Mg}\tau_O}{\tau_{Mg}+\tau_O}\alpha_{Mg}\alpha_O \tag{3}$$

where τ is the ionization energy of the atoms, which can be obtained from the NIST Atomic Spectra Database (Kramida et al. 2021). α are the static dipole polarisabilities, where α are 71.2, 2.92, and 87.0 au for the ^1S_g, ^1P_u, and ^3P_u states of Mg (Mérawa et al. 2001) and 5.35, 5.43, and 5.76 au for the ^3P_g, ^1D_g, and ^1S_g states of O (Medved, Fowler & Hutson 2000). C_5 is the quadrupole–quadrupole electrostatic interaction and can be estimated by fitting *ab initio* points. A cubic spline was used to interpolate the *ab initio* points.

2.2 The photodissociation cross-section

The cross-section for a bound-free transition from the initial electronic state characterized by Λ" to the final state Λ' is given by

$$\sigma^{\Lambda''\to\Lambda'}\left(E_{ph}\right) = 2\pi^2\alpha\frac{\mathrm{d}f^{\Lambda''\to\Lambda'}}{\mathrm{d}E_{ph}}, \tag{4}$$

where E_{ph} is the photon energy and m is the mass of the electron. $\alpha = e^2/\hbar c$ is the fine-structure constant and e, $\hbar$, c are the electric charge of an electron, the reduced Planck constant, and the speed of light, respectively. The continuum differential oscillator strength is defined by

$$\frac{\mathrm{d}f^{\Lambda''\to\Lambda'}}{\mathrm{d}E_{ph}} = \frac{2m}{3\hbar^2}E_{ph}|\langle\chi_{k'J'}(R)|D(R)|\chi_{v''J''}(R)\rangle|^2. \tag{5}$$

Therefore, if the photon energy and TDMs are in atomic units, the state-resolved cross-sections in cm^2 for a transition can be expressed by

$$\sigma_{v''J''}(E_{ph}) = 2.689\times10^{-18} \times gE_{ph}\sum_{J'}\left(\frac{1}{2J''+1}S_{J'}\left|D_{k'J',\,v''J''}\right|^2\right), \tag{6}$$

where $S_{J'}$ are the Hönl-London factors (Hansson & Watson 2005; Watson 2008) and g is the degeneracy factor and given by

$$g = \frac{2-\delta_{0,\Lambda'+\Lambda''}}{2-\delta_{0,\Lambda''}}. \tag{7}$$

The electric dipole transition moment function is expressed by

$$D_{k'J',\,v''J''} = \langle\chi_{k'J'}(R)|D(R)|\chi_{v''J''}(R)\rangle, \tag{8}$$

where $D(R)$ are the TDMs from *ab initio* calculations, $\chi_{k'J'}(R)$ are the energy-normalized continuum wave functions, and $\chi_{v''J'}(R)$ are the bound wave functions by solving the radial Schrödinger equation. The renormalized Numerov method was used to obtain the continuum and bound wave functions (Johnson 1977, 1978). The wave functions were calculated over the internuclear ranges from 0.5 to 100Å and the scanning step was 0.001Å.

The population of rovibrational levels of the initial state can be calculated using a Boltzmann distribution. Thus, the corresponding photodissociation cross-sections in the LTE can be expressed as a function of both the gas temperature T_g and the wavelength of the incident photon λ

$$\sigma\left(\lambda, T_g\right) = \frac{\sum_{v''J''}(2J''+1)\exp\left(-|E_{v''J''}-E_{00}|/k_BT_g\right)\sigma_{v''J''}}{Q\left(T_g\right)}, \tag{9}$$

where $Q(T_g)$ is the rovibrational partition function and given by

$$Q\left(T_g\right) = \sum_{v''J''}\left(2J''+1\right)\exp\left(-|E_{v''J''}-E_{00}|/k_BT_g\right), \tag{10}$$

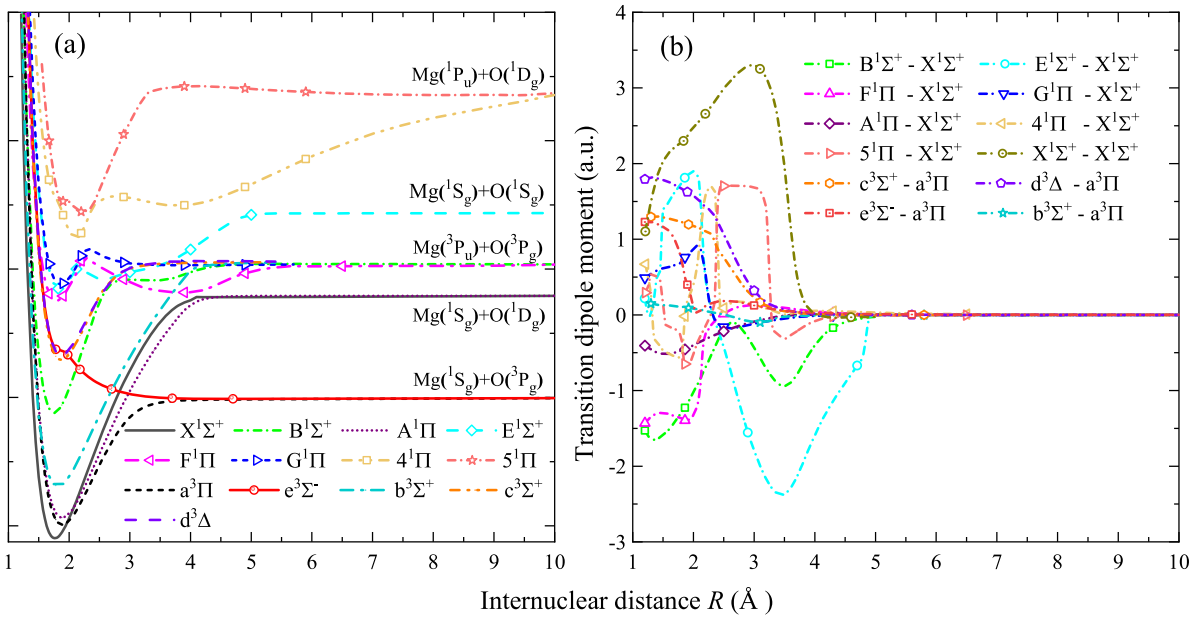

Figure 1. *Ab initio* points of (a) the PECs of each considered MgO molecular state and (b) the TDMs for the transition from the $X^1\Sigma^+$ and $a^3\Pi$ states.

where $E_{v''J''}$ is the energy of an electronic state with quantum numbers v'', J'', and k_B is the Boltzmann constant.

2.3 Photodissociation rates

The photodissociation rate of a molecule exposed to a radiation field is given by

$$k(T) = \int \sigma(\lambda, T)\, I(\lambda)\, \mathrm{d}\lambda, \tag{11}$$

where $I(\lambda)$ is the photon intensity from the radiation field summed over all incident angles. The average intensity of the interstellar radiation field can be estimated from the number and distribution of hot stars in the Galaxy, combined with a model for the dust distribution and its extinction of the stellar radiation. These radiation fields are severely depleted for wavelengths shorter than 91.2 nm due to the ionization threshold of atomic H (Draine 1978). For the wavelengths within the 91.2–200 nm, the wavelength dependence ultraviolet intensity was defined by Draine (1978)

$$I(\lambda) = 3.2028 \times 10^{13}\lambda^{-3} - 5.1542 \times 10^{15}\lambda^{-4} + 2.0546 \times 10^{17}\lambda^{-5}, \quad 91.2\,\mathrm{nm} < \lambda < 200\,\mathrm{nm} \tag{12}$$

For the interstellar flux at longer wavelengths between 200 and 2000 nm, an extension was proposed by van Dishoeck & Black (1982)

$$I(\lambda) = 3.67 \times 10^{4}\lambda^{0.7}, \quad 200\,\mathrm{nm} < \lambda < 2000\,\mathrm{nm} \tag{13}$$

where the unit of the wavelength, λ, is nm and the radiation intensity has the unit of photos·cm^{-2}·s^{-1}·nm^{-1}.

The field near to a star is dominated by the blackbody radiation, the emitted radiation intensity at the temperature T_b is calculated by

$$I_b(\lambda, T_b) = \frac{8\pi c/\lambda^4}{\exp(hc/k_B T_b \lambda) - 1}, \tag{14}$$

where h is the Planck constant.

In reality, stellar spectra are not similar to those generated by black bodies and contain many emission or absorption lines. As for the solar radiation field, it was measured by the observations with the Solar Ultraviolet Measurements of Emitted Radiation spectrograph between 67 and 160.9 nm (Curdt et al. 2001) and the *Solar Radiation and Climate Experiment* satellite for longer wavelengths (Harder et al. 2021). The solar radiation field was required to be normalized to match the energy intensity of the Draine field between 91.2 and 200 nm, and thus a scale factor of 37 700 should be selected (Heays et al. 2017).

3 RESULTS AND DISCUSSION

3.1 Potential energy and transition moment curves

The PECs of twelve electronic states considered in photodissociation processes were investigated theoretically and shown in Fig. 1(a). These states correlate to five dissociation limits, as shown in Table 1. Based on the selected basis set, active space, and state-averaged calculation, the $4^1\Pi$ state correlates to the Mg (^1P_u) + O (^1D_g) dissociation limit instead of Mg (^1S_g) + O (^1S_g) calculated by Maatouk et al. (2010). For the $X^1\Sigma^+$, $B^1\Sigma^+$, $A^1\Pi$, $a^3\Pi$, $b^3\Sigma^+$, $c^3\Sigma^+$, and $d^3\Delta$ states, they have been investigated in our previous work (Bai et al. 2020), where the $X^1\Sigma^+$ state is found to support 96 vibrational levels, with a maximum rotational level $J'' = 287$. For other bound states, the spectroscopic parameters of the $F^1\Pi$, $E^1\Sigma^+$, $G^1\Pi$, and $4^1\Pi$ states were obtained by fitting the vibrational energies from the solution of the Schrödinger equation of nuclear motion and shown in Table 2. The results are consistent with the earlier experimental and theoretical ones. For the $F^1\Pi$ and $G^1\Pi$ states, our results are more consistent with the latest experimental data than previous theoretical ones due to the core–valence correlation and scalar relativistic effect included in our calculations. Fig. 1(b) shows the TDMs for the transitions from the $X^1\Sigma^+$ and $a^3\Pi$ states to other states. The comparison with earlier theoretical results is shown in Fig. 2, which reveals our TDMs for the $A^1\Pi \leftarrow X^1\Sigma^+$, $a^3\Pi \leftarrow c^3\Sigma^+$,

Table 1. The asymptotic separated-atom limits for the molecular states involved in the MgO photodissociation process.

Molecular states	Separated-atom atomic states	Dissociation limit (cm^{-1}) Experiment.[a]	Theory.	$C_5/10^4$	C_6
$a^3\Pi$	$Mg(2p^6 3s^2\ ^1S_g) + O(2s^2 2p^4\ ^3P_g)$	0	0	9.27	102.82
$e^3\Sigma^-$				6.81	102.82
$X^1\Sigma^+$	$Mg(2p^6 3s^2\ ^1S_g) + O(2s^2 2p^4\ ^1D_g)$	15 867.86	15 830.88[b]	5.47	104.36
$A^1\Pi$				10.54	104.36
$b^3\Sigma^+$	$Mg(3s3p\ ^3P_u) + O(2s^2 2p^4\ ^3P_g)$	22 069.97	21 850.41[b]	38.44	125.64
$c^3\Sigma^+$				36.37	125.64
$d^1\Delta$				31.36	125.64
$B^1\Sigma^+$				5.88	125.64
$F^1\Pi$				20.09	125.64
$G^1\Pi$				14.24	125.64
$E^1\Sigma^+$	$Mg(2p^6 3s^2\ ^1S_g) + O(2s^2 2p^4\ ^1S_g)$	33 792.58	28 679.48	76.19	110.70
$4^1\Pi$	$Mg(3s3p\ ^1P_u) + O(2s^2 2p^4\ ^1D_g)$	50 919.13	47 140.08	58.12	4.28
$5^1\Pi$				40.72	4.28

Notes. [a]Experimental data from NIST Atomic Spectra Database (Kramida et al. 2021).
[b]Theoretical data from Bai et al. (2020).

Table 2. Spectroscopic parameters of four electronic states of MgO obtained by the icMRCI+Q method.

State			T_e/cm^{-1}	ω_e/cm^{-1}	$\omega_e x_e$	B_e	$\alpha_e/\times 10^{-3} cm^{-1}$	r_e/Å
$F^1\Pi$	This work	Inner wall	36 955.05	714.59	9.9443	0.5506	3.35	1.784
	Expt.[a]			711	6.9	0.562	0.0063	1.77
	Expt.[b]			705	4.5	0.563	5.5	1.766
	Expt.[c]		37 922	696		0.5590		1.772
	Calc.[d]		37 322.6	699.2	5.12	0.5503	5.58	1.786
	This work	Outer wall		124.50	1.3201	0.1176	2.28	3.781
	Calc.[d]			162.1	4.86	0.1194	5.06	3.836
$E^1\Sigma^+$	This work	Inner wall	38 842.31	689.30	25.3202	0.5195	6.91	1.842
	Expt.[c]			705		0.524		1.829
	Calc.[d]		39 113.1	698.1	10.95	0.5201	8.67	1.837
	This work	Outer wall		279.91	5.1438	0.2676	0.5426	2.560
	Calc.[d]			196.4	13.30	0.22 163	39.42	2.815
$G^1\Pi$	This work	Inner wall	39 592.19	644.27	0.2943	0.5125	12.61	1.859
	Expt.[c]					0.522		1.834
	Calc.[d]		40 364.1	621.369	2.59	0.5029	6.80	1.869
	This work	Outer wall		30.8621	1.9341	0.1096	0.73	3.965
	Calc.[d]			31.0	2.33	0.1103	7.68	3.990
$4^1\Pi$	This work		44 403.05	884.38	30.9065	0.3926	2.74	2.116
	Calc.[d]		44 987.9	891.8	1.31	0.3724	7.99	2.172

Notes. [a]Experiment (Wang & Breckenridge 2006).
[b]Experiment (Bellert et al. 2003).
[c]Experiment (Huber & Herzberg 1979).
[d]Calculation (Maatouk et al. 2010).

$a^3\Pi \leftarrow d^3\Delta$, and $B^1\Sigma^+ \leftarrow X^1\Sigma^+$ transitions are in agreement with the results from previous theories and they are reliable.

3.2 State-resolved and LTE cross-sections

The state-resolved cross-sections for the transitions from the rovibrational level $v''=0, J''=0$ of the $X^1\Sigma^+$ and $a^3\Pi$ states to other excited states were computed and shown in Fig. 3. These cross-sections display several nodes, antinodes, and quasi-periodic behaviour due to the oscillatory character of the continuum wave functions (Gay et al. 2012). The interstellar radiation field is most intense between the H Lyman limit and H Lyman α (Draine 1978). In this particular environment, the transition from the ground state to the $5^1\Pi$ state may play an important role. The transition $G^1\Pi \leftarrow X^1\Sigma^+$ plays an important role in the middle ultraviolet waveband. It is due to the fact that the $G^1\Pi$ state has a shallow well compared with the same dissociation limit of the $F^1\Pi$ and $B^1\Sigma^+$ states, which leads to larger cross-sections at the same wavelength. For the transitions between triplet states, the cross-sections are dominated by the $e^3\Sigma^- \leftarrow a^3\Pi$ transition because of the almost repulsive potential of the $e^3\Sigma^-$ state, and the cross-sections reach a maximum of 1.05×10^{-16} cm^2 at the wavelength of 3704 Å. Other transitions, such as the $B^1\Sigma^+ \leftarrow X^1\Sigma^+$, $A^1\Pi \leftarrow X^1\Sigma^+$, $X^1\Sigma^+ \leftarrow X^1\Sigma^+$, $b^3\Sigma^+ \leftarrow a^3\Pi$, $c^3\Sigma^+ \leftarrow a^3\Pi$, and $d^3\Delta \leftarrow a^3\Pi$ transitions, contribute little to the cross-sections. It is

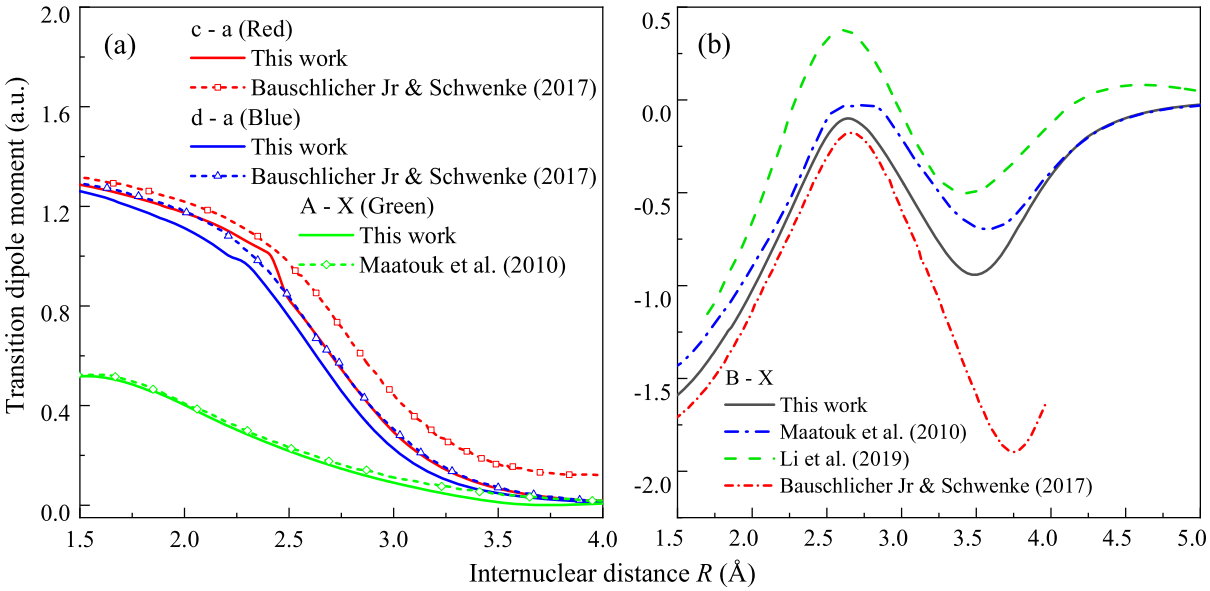

Figure 2. The comparisons of the TDMs for (a) the $A^1\Pi \leftarrow X^1\Sigma^+$, $a^3\Pi \leftarrow c^3\Sigma^+$, and $a^3\Pi \leftarrow d^3\Delta$ transitions with those from Maatouk et al. (2010) and Bauschlicher Jr & Schwenke (2017) and (b) the $B^1\Sigma^+ \leftarrow X^1\Sigma^+$ transition with that from Maatouk et al. (2010); Li et al. (2019), and Bauschlicher Jr & Schwenke (2017).

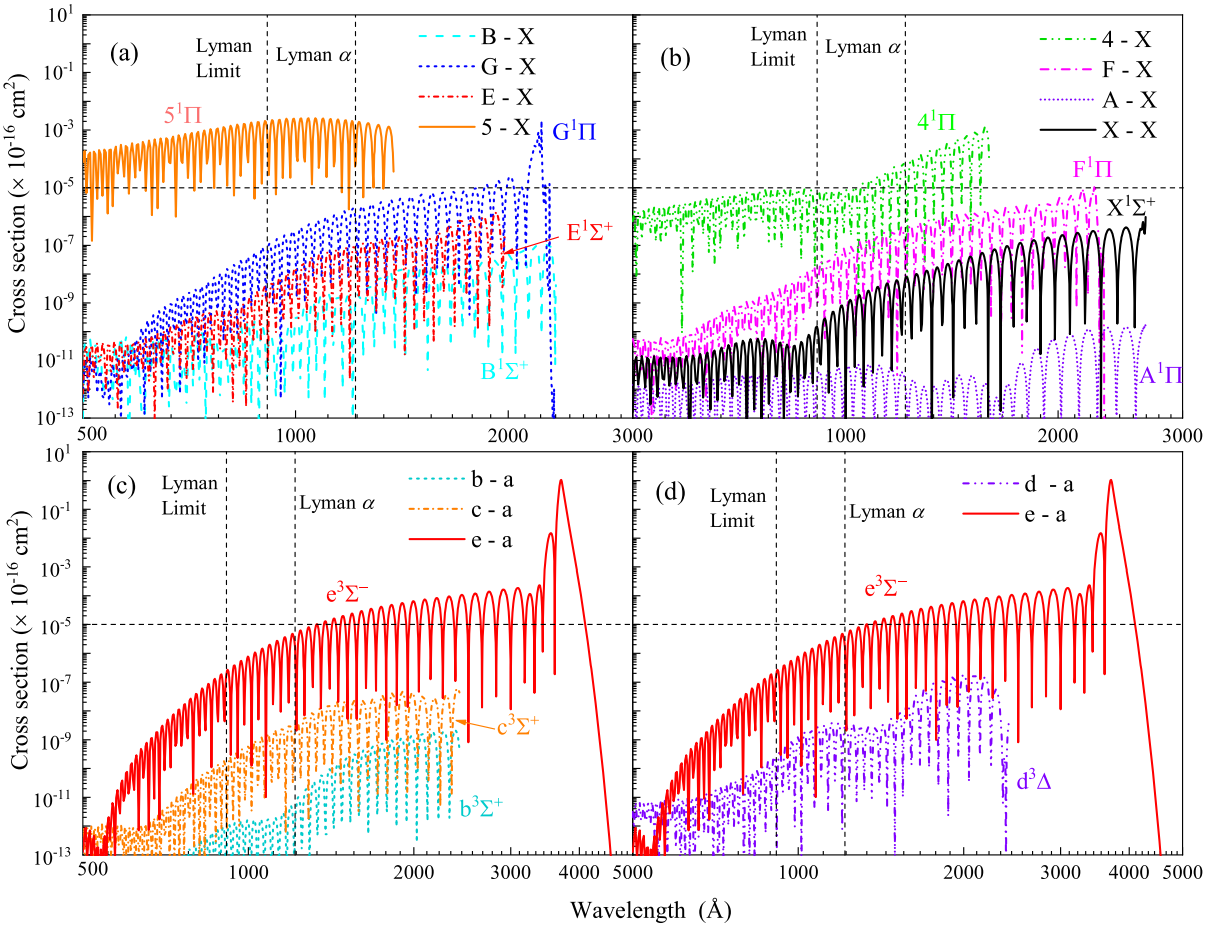

Figure 3. The state-resolved cross-sections for the transitions from the rovibrational level $v'' = 0$, $J'' = 0$ of the (a-b) $X^1\Sigma^+$ and (c-d) $a^3\Pi$ states.

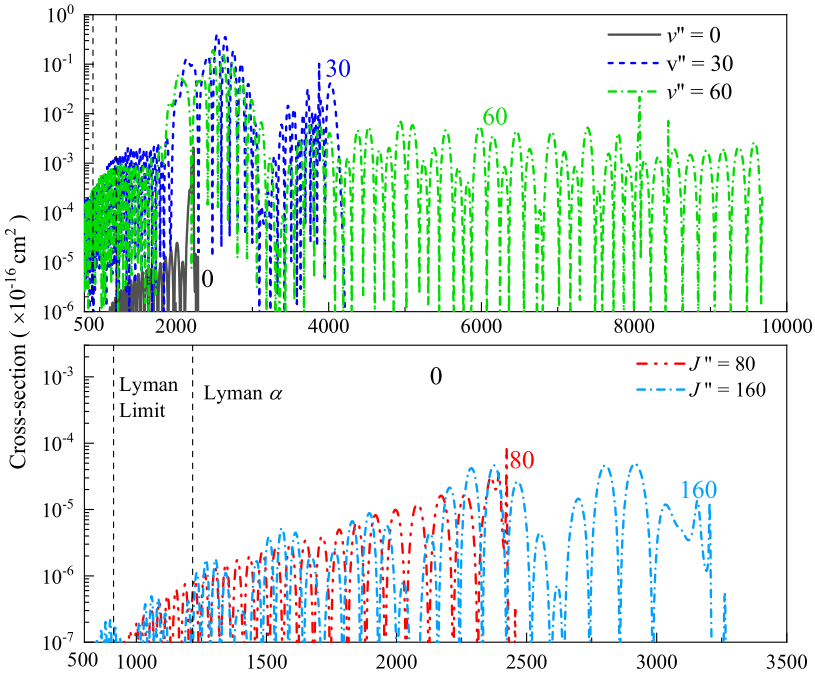

Figure 4. The state-resolved cross-sections for the $G^1\Pi \leftarrow X^1\Sigma^+$ transition for (a) $v'' = 0$ and select J'' and (b) $J'' = 0$ and select v''.

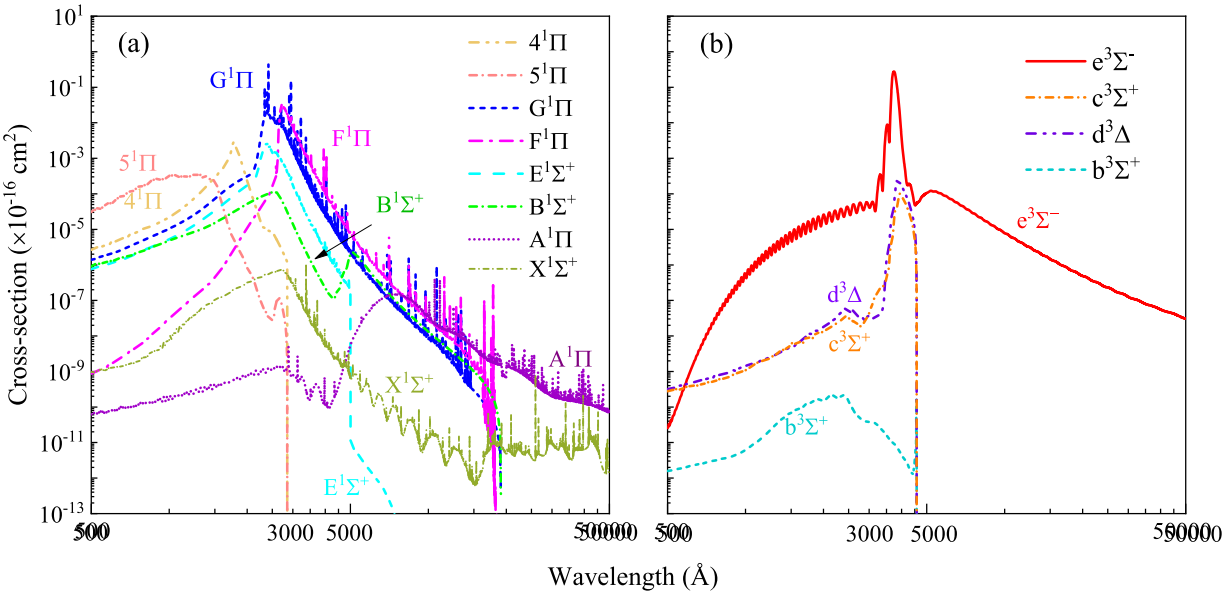

Figure 5. The LTE cross-sections at 3000 K for the transition from (a) the $X^1\Sigma^+$ and (b) $a^3\Pi$ states to the other states.

mainly due to the lower dissociation limits or deeper potential wells of these high states.

Due to the generally large state-resolved cross-sections of the $G^1\Pi \leftarrow X^1\Sigma^+$ transition in Fig. 3(a), the state-resolved cross-sections for the transitions from vibrational level $v'' = 0$ with different J'' and from rotational level $J'' = 0$ with different v'' of the ground state to the $G^1\Pi$ state were calculated and shown in Fig. 4. As the vibrational and/or rotational level increases, the threshold wavelength transition increases, because the wave function samples a higher and wider part of the potential of the ground state as the vibrational/rotational level increases for a specific rotational/vibrational level. Similar trends can be found for the other transitions studied in this work.

The LTE cross-sections were computed by equation (9) from 500 to 10 000 K for the transition from the rovibrational level of the $X^1\Sigma^+$ and $a^3\Pi$ states to the other states, where a comparison of the LTE cross-sections at 3000 K for each transition is shown in Fig. 5. For the photodissociation by the transitions between the singlet states, the photolysis through the $5^1\Pi$ state is dominant at short wavelengths, which is consistent with the previous analysis on the state-resolved cross-sections. With the wavelength increasing, the photodissociation processes for the $G^1\Pi \leftarrow X^1\Sigma^+$ and $F^1\Pi \leftarrow X^1\Sigma^+$ transitions play a key role. Due to the deep well of the $A^1\Pi$ and $X^1\Sigma^+$ states, the energy-normalized continuum wave functions are smaller near the equilibrium internuclear distance of the ground state,

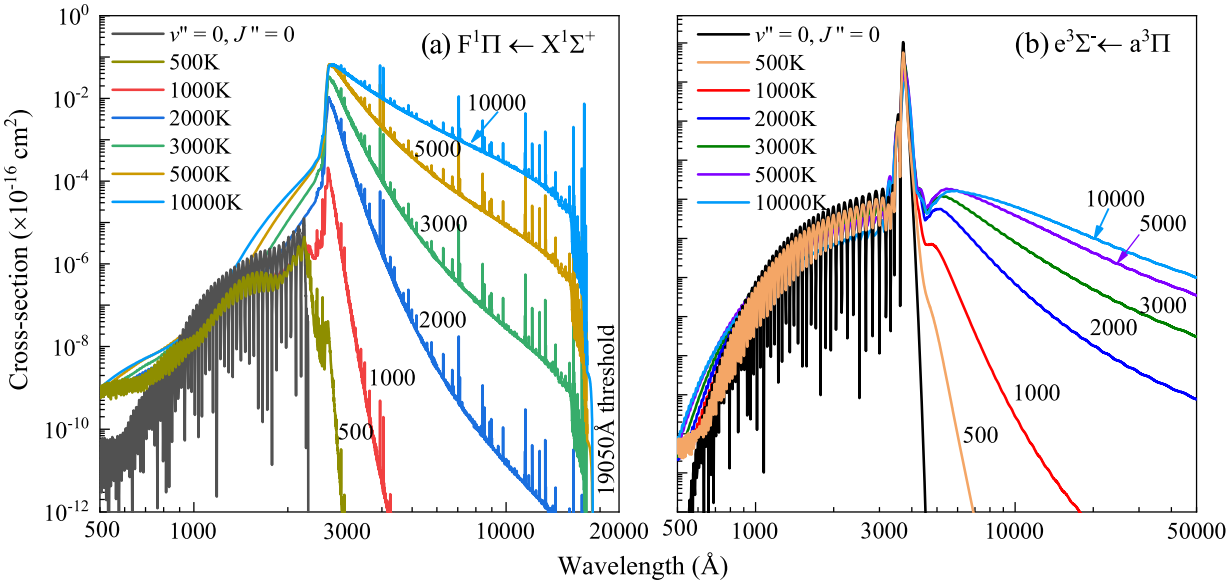

Figure 6. The LTE cross-sections for (a) the $F^1\Pi \leftarrow X^1\Sigma^+$ and (b) $e^3\Sigma^- \leftarrow a^3\Pi$ transitions at various kinetic temperatures and the $v" = 0, J" = 0$ state-resolved cross-sections included for a comparison.

leading to the small cross-sections. The photodissociation cross-sections by the transitions between the triplet states are displayed in Fig. 5(b), which shows the photodissociation of MgO can be mainly achieved through the $e^3\Sigma^- \leftarrow a^3\Pi$ process. Because the $F^1\Pi \leftarrow X^1\Sigma^+$ and $e^3\Sigma^- \leftarrow a^3\Pi$ transitions are dominant for the majority of wavelengths in Fig. 5, the LTE cross-sections for these two transitions at various kinetic temperatures are displayed in Fig. 6. As the temperature increases, the cross-sections for the $F^1\Pi \leftarrow X^1\Sigma^+$ transition increase dramatically between 5000 and 19 050 Å, due to the photodissociation threshold. For the $e^3\Sigma^- \leftarrow a^3\Pi$ transition, the similar tendency is found in the cross-sections between 5000 and 50 000 Å.

3.3 Photodissociation rates

We calculated the LTE photodissociation rates of MgO in the interstellar, solar, and blackbody radiation fields, as shown in Fig. 7. For the radiation field generated by a blackbody, the temperature of the gas was assumed to be the same as the temperature of the radiation field. The results show the LTE rates in all studied radiation field increase with the temperature of the gas increasing. The rates in the interstellar radiation field are smaller than those in the solar radiation field, because compared with the solar field, the interstellar radiation field is only dominated in the wavelength range of 91.2–200 nm., In addition, the photodissociation of MgO is dominated by the $F^1\Pi \leftarrow X^1\Sigma^+$ and $e^3\Sigma^- \leftarrow a^3\Pi$ transitions in all the radiation fields. The photodissociation rates of other diatomic molecules (e.g. NO, AlH, LiH, MgH, NaH, and NaCl) in the interstellar and solar radiation fields have been investigated by Heays et al. (2017), our rates are of a similar order of magnitude to these results.

In order to clearly understand the direct photodissociation mechanism in the blackbody radiation field, the proportion of each transition rate in the total rate was computed and displayed in Fig. 8. According to equation (14), the radiation intensity emitted by a low-temperature blackbody is strong at the long wavelengths, and the transition to the $e^3\Sigma^-$ state also plays a key role at the long wavelengths. As a result, the photodissociation via the $e^3\Sigma^-$ state is the key destruction pathway at low temperatures (< 3000 K). With the temperature increasing, the transition from the high excited state, $F^1\Pi$, is dominant for the photolysis (>6400 K), followed by the transitions from the $G^1\Pi$ and $E^1\Sigma^+$ states. However, the $5^1\Pi$, $4^1\Pi$, $B^1\Sigma^+$, $b^3\Sigma^+$, $A^1\Pi$, and $X^1\Sigma^+$ states have little effect on the photodissociation due to their deep potential wells. Such phenomenon also exists in the interstellar and solar radiation fields.

4 CONCLUSIONS

In this work, we have calculated the accurate cross-sections and rates for the direct photodissociation of MgO through the transitions from the $5^1\Pi$, $4^1\Pi$, $F^1\Pi$, $G^1\Pi$, $A^1\Pi$, $E^1\Sigma^+$, and $B^1\Sigma^+$states to the $X^1\Sigma^+$ state and from the $b^3\Sigma^+$, $c^3\Sigma^+$, and $d^3\Delta$ states to the $a^3\Pi$ state using the *ab initio* PECs and TDMs. The state-resolved cross-sections have been computed for the transitions from all rovibrational levels of the $X^1\Sigma^+$ and $a^3\Pi$ states to all rotational levels of the other states. Assuming a Boltzmann distribution of rovibrational levels in the initial state, the LTE cross-sections have been calculated for the gas temperature ranging from 500 to 10 000 K. The calculated cross-sections can be used to compute the photodissociation rate in the early universe and interstellar environment. Thus, the rates in the interstellar, solar, and blackbody radiation fields have been computed as well. The results show that the rates increase in all studied radiation fields with the gas temperature increasing, where the rates in the interstellar radiation field are smaller than those in the solar radiation field. The photodissociation of MgO is dominated by the $e^3\Sigma^- \leftarrow a^3\Pi$ and $F^1\Pi \leftarrow X^1\Sigma^+$ transitions in the studied radiation fields. The $e^3\Sigma^- \leftarrow a^3\Pi$ transition is found to be dominant significantly at the low-temperature radiation field, while the $F^1\Pi \leftarrow X^1\Sigma^+$ transition dominates for the high-temperature field. The calculated rates in different radiation fields can further be used to investigate the evolution and abundance of MgO molecule in every type of astrophysical region (e.g. clouds, envelopes, and discs). Meanwhile, they can also be folded into chemical network models to improve the description of the magnesium chemistry.

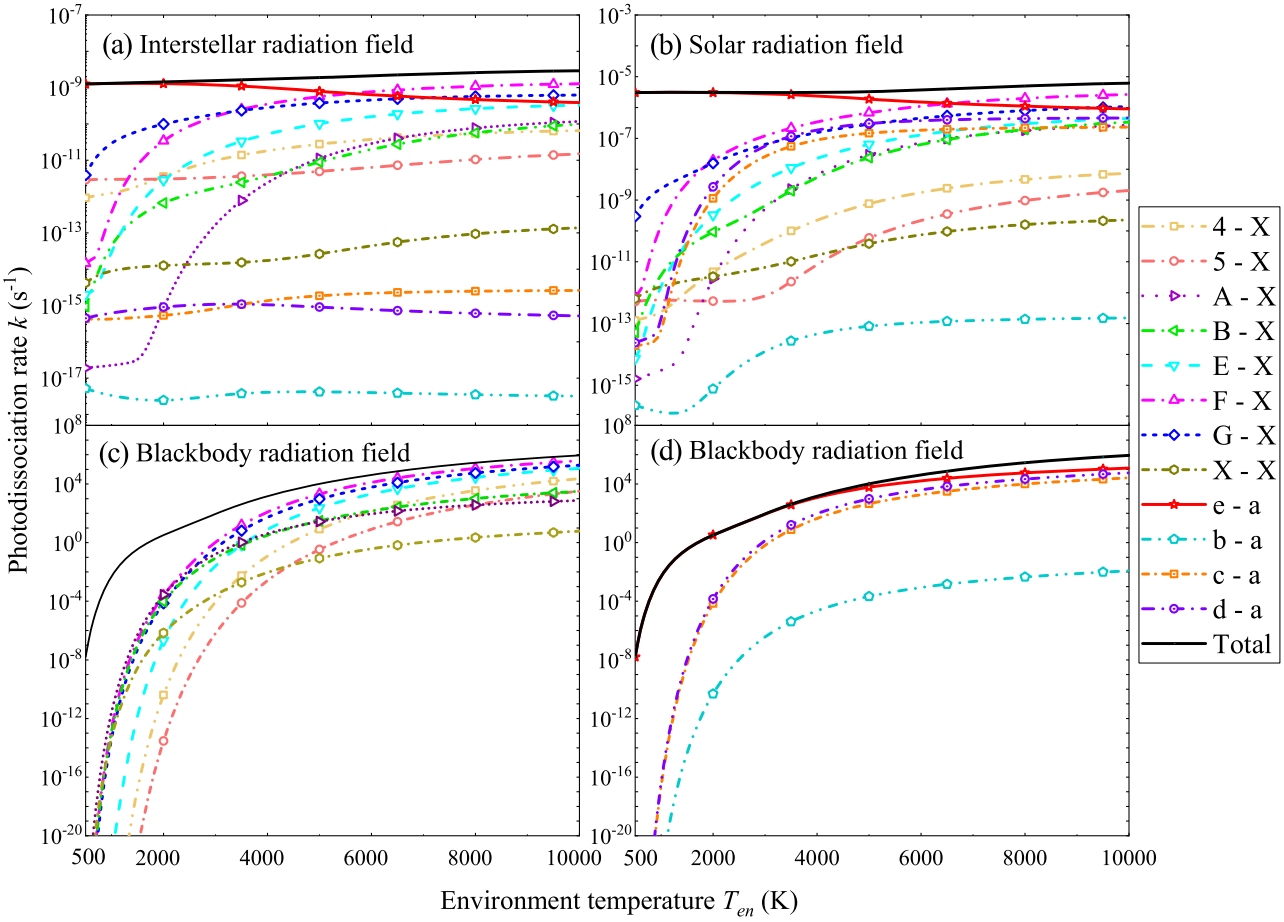

Figure 7. The LTE photodissociation rates in the (a) interstellar, (b) solar, and (c and d) blackbody radiation fields where the kinetic and radiant temperatures are equal.

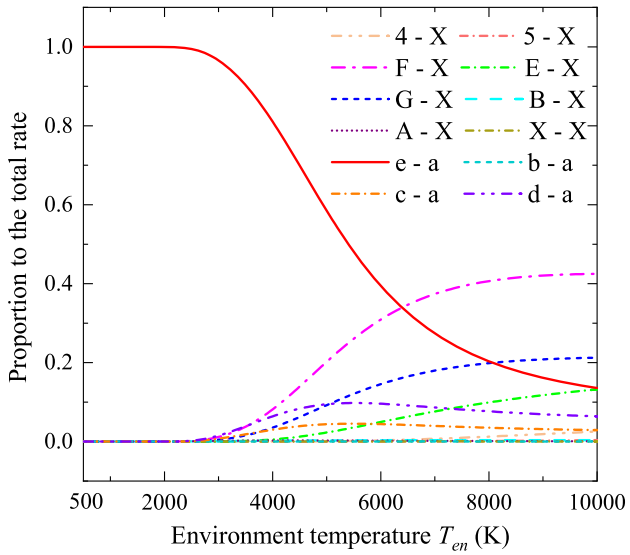

Figure 8. The proportion of photolysis rate for each transition to the total rate in the blackbody radiation field.

ACKNOWLEDGEMENTS

This work is sponsored by the National Natural Science Foundation of China under grant no. 51336002, 51421063. The scientific calculations in this paper have been done on the HPC Cloud Platform of Shandong University.

DATA AVAILABILITY STATEMENT

All cross-section data can be obtained online at https://dr-zhi-qin.github.io/personal/Database.html. The data underlying this article are available in the article and its online supplementary material includes the rate coefficients in the interstellar, solar, and blackbody radiation fields (corresponding to Fig. 7).

REFERENCES

Anderson J. G., Barth C. A., 1971, J. Geophys. Res., 76, 3723
Bai T., Qin Z., Liu L., 2020, J. Quant. Spectrosc. Radiat. Transfer, 107086
Bauschlicher C. W. Jr, Schwenke D. W., 2017, Chem. Phys. Lett., 683, 62
Bellert D., Burns K. L., Van-Oanh N.-T., Wang J., Breckenridge W. H., 2003, Chem. Phys. Lett., 381, 381
Bennett C. J., Pirim C., Orlando T. M., 2013, Chem. Rev., 113, 9086
Berezhnoy A. A., 2010, Adv. Space Res., 45, 70
Berezhnoy A. A., 2013, Icarus, 226, 205

Berezhnoy A. A., 2018, Icarus, 300, 210
Berezhnoy A. A. et al., 2014, Planet. Space Sci.., 96, 90
Correira J., Aikin A. C., Grebowsky J. M., Pesnell W. D., Burrows J. P., 2008, Geophys. Res. Lett., 35, L06103
Curdt W., Brekke P., Feldman U., Wilhelm K., Dwivedi B. N., Schuähle U., Lemaire P., 2001, A&A, 375, 591
Draine B. T., 1978, ApJ Suppl. Ser., 36, 595
El-Qadi W. H., Stancil P. C., 2013, ApJ, 779, 97
Gay C. D., Abel N. P., Porter R. L., Stancil P. C., Ferland G. J., Shaw G., Van Hoof P. A. M., Williams R. J. R., 2012, ApJ, 746, 78
Hansson A., Watson J. K. G., 2005, J. Mol. Spectrosc., 233, 169
Harder J., Snow M., Woods T., 2021. Solar Spectral Irradiance Data. Available at: https://lasp.colorado.edu/home/sorce/data/ssi-data/
Heays A. N., Bosman A. D., Van Dishoeck E. F., 2017, A&A, 602, A105
Huber K. P., Herzberg G., 1979, Molecular Spectra and Molecular Structure. Elsevier, New York
Johnson B. R., 1977, J. Chem. Phys., 67, 4086
Johnson B. R., 1978, J. Chem. Phys., 69, 4678
Kramida A., Ralchenko Y., Reader J., NIST ASD Team, 2021, NIST Atomic Spectra Database (version 5.8). Available at: https://physics.nist.gov/asd
Lee H.-H., Herbst E., Pineau des Forets G., Roueff E., Le Bourlot J., 1996, A&A, 311, 690
Li H. Y., Tennyson J., Yurchenko S. N., 2019, MNRAS, 486, 2351
Li X., Millar T. J., Walsh C., Heays A. N., Dishoeck E. F. V., 2014, A&A, 568, 689
Maatouk A., Ben Houria A., Yazidi O., Jaidane N., Hochlaf M., 2010, J. Chem. Phys., 133, 144302
Mashonkina L., 2013, A&A, 550, A28
McClintock W. E. et al., 2009, Science, 324, 610
Mcmillan E. C., Shen G., Mccann J. F., Mclaughlin B. M., Stancil P. C., 2016, J. Phys. B: At. Mol. Opt. Phys., 49, 084001
Medved M., Fowler P. W., Hutson J. M., 2000, Molecular Physics, 98, 453
Sarantos M. et al., 2011, Planet. Space Sci., 59, 1992
Mérawa M., Bégué D., Rérat M., Pouchan C., 2001, Chem. Phys. Lett., 334, 403
Miyake S., Gay C. D., Stancil P. C., 2011, ApJ, 735, 21
Pattillo R. J., Cieszewski R., Stancil P. C., Forrey R. C., Babb J. F., Mccann J. F., Mclaughlin B. M., 2018, ApJ, 858, 10
Plane J. M. C., Whalley C. L., 2012, J. Phys. Chem. A, 116, 6240
Sarantos M., Killen R. M., Mcclintock W. E., Bradley E. T., Vervack R. J., Benna M., Slavin J. A., 2011, Planet. Space Sci., 59, 1992
Stancil P. C., Kirby K., Sannigrahi A. B., Buenker R. J., Hirsch G., Gu J. P., 1997, ApJ, 486, 574
Sternberg A., Dalgarno A., 1995, ApJ Suppl. Ser., 99, 565
Stockstill-Cahill K. R., McCoy T. J., Nittler L. R., Weider S. Z., Hauck S. A., II, 2012, J. Geophys. Res.: Planets, 117, E00L15
Valiev R. R., Berezhnoy A. A., Gritsenko I. S., Merzlikin B. S., Cherepanov V. N. T. K., Whler C., 2020, A&A, 633, A39
Valiev R. R., Berezhnoy A. A., Minaev B. F., Chernov V. E., Cherepanov V. N., 2016, Russ. Phys. J., 59, 536
Valiev R. R., Berezhnoy A. A., Sidorenko A. D., Merzlikin B. S., Cherepanov V. N., 2017, Planet. Space Sci., 145, 38
van Dishoeck E. F., Black J. H., 1982, ApJ, 258, 533
Wang J., Breckenridge W. H., 2006, J. Chem. Phys., 124, 417
Watson J. K. G., 2008, J. Mol. Spectrosc., 252, 5
Weck P. F., Stancil P. C., Kirby K., 2003, ApJ, 582, 1263
Werner H.-J. et al., 2015, Molpro, Version 2015.1, A Package of Ab Initio Programs. TTI GmbH Stuttgart, Stuttgart, Germany

SUPPORTING INFORMATION

Supplementary data are available at *MNRAS* online.

Supplementary Material.zip

Please note: Oxford University Press is not responsible for the content or functionality of any supporting materials supplied by the authors. Any queries (other than missing material) should be directed to the corresponding author for the article.

This paper has been typeset from a TEX/LATEX file prepared by the author.